JACS
JOURNAL OF THE AMERICAN CHEMICAL SOCIETY

Article

pubs.acs.org/JACS

Ice Nucleation Efficiency of Hydroxylated Organic Surfaces Is Controlled by Their Structural Fluctuations and Mismatch to Ice

Yuqing Qiu,[†] Nathan Odendahl,[†] Arpa Hudait,[†] Ryan Mason,[‡] Allan K. Bertram,[‡] Francesco Paesani,[§] Paul J. DeMott,[∥] and Valeria Molinero*[,†]

[†]Department of Chemistry, The University of Utah, 315 South 1400 East, Salt Lake City, Utah 84112-0850, United States
[‡]Department of Chemistry, University of British Columbia, Vancouver, British Columbia V6T 1Z1, Canada
[§]Department of Chemistry and Biochemistry, University of California, San Diego, La Jolla, California 92093, United States
[∥]Department of Atmospheric Science, Colorado State University, Fort Collins, Colorado 80523-1371, United States

ABSTRACT: Heterogeneous nucleation of ice induced by organic materials is of fundamental importance for climate, biology, and industry. Among organic ice-nucleating surfaces, monolayers of long chain alcohols are particularly effective, while monolayers of fatty acids are significantly less so. As these monolayers expose to water hydroxyl groups with an order that resembles the one in the basal plane of ice, it was proposed that lattice matching between ice and the surface controls their ice-nucleating efficiency. Organic monolayers are soft materials and display significant fluctuations. It has been conjectured that these fluctuations assist in the nucleation of ice. Here we use molecular dynamic simulations and laboratory experiments to investigate the relationship between the structure and fluctuations of hydroxylated organic surfaces and the temperature at which they nucleate ice. We find that these surfaces order interfacial water to form domains with ice-like order that are the birthplace of ice. Both mismatch and fluctuations decrease the size of the preordered domains and monotonously decrease the ice freezing temperature. The simulations indicate that fluctuations depress the freezing efficiency of monolayers of alcohols or acids to half the value predicted from lattice mismatch alone. The model captures the experimental trend in freezing efficiencies as a function of chain length and predicts that alcohols have higher freezing efficiency than acids of the same chain length. These trends are mostly controlled by the modulation of the structural mismatch to ice. We use classical nucleation theory to show that the freezing efficiencies of the monolayers are directly related to their free energy of binding to ice. This study provides a general framework to relate the equilibrium thermodynamics of ice binding to a surface and the nonequilibrium ice freezing temperature and suggests that these could be predicted from the structure of interfacial water.

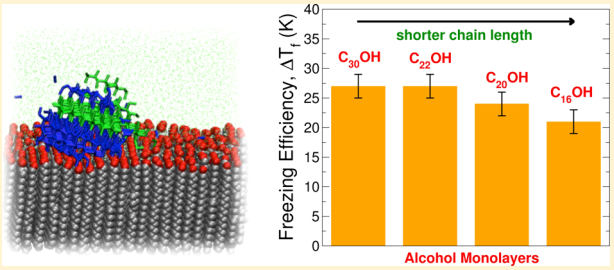

1. INTRODUCTION

Ice nucleation is key for climate because of its paramount role in cloud formation,[1−5] electrification,[6,7] and precipitation.[8−11] Atmospheric water droplets can be supercooled down to −38 °C in the absence of ice-nucleating surfaces.[12] Crystallization of ice in the atmosphere, however, is usually triggered at warmer temperatures by minerals, soot, and organic and biological materials present in aerosols.[13−17] Organic[18−20] and biological[21−23] compounds are among the best ice-nucleating agents, but it is not yet established which characteristics of these surfaces control their ice-freezing efficiency.

Many organic and biological surfaces expose to water surfaces with hydroxyl (OH) groups ordered to resemble planes of the ice lattice. Monolayers of *n*-alky alcohols[24−34] and fatty acids[24,26,34] as well as the binding site of ice-nucleating proteins (INP)[23,35−39] are paradigmatic examples of such surfaces. Among nonbiological surfaces, monolayers of long chain alcohols are particularly efficient in promoting heterogeneous nucleation of ice.[24−33] Experimental studies of ice freezing by alcohol monolayers demonstrate that the freezing temperature increases with the length of the hydrocarbon tail.[24,27,28,33] The authors of these pioneering studies proposed that the heterogeneous freezing temperature of ice is controlled by matching between the crystalline position of the hydroxyl moieties in the monolayer and the undercoordinated water molecules in the basal surface of ice.[33] Nevertheless, there is not yet a predictive relationship between the order of the hydroxyl groups in the nucleating surface and the ice-freezing temperature. Finding that relation is the first goal of this work.

Unlike mineral surfaces, organic surfaces can be soft. It has been conjectured that fluctuations of the surface could compensate for the lattice mismatch of alcohol monolayers to ice, increasing their freezing efficiency.[25,40] However, recent simulation studies of water freezing on kaolinite found that mobility of hydroxyls groups on a fixed, flat, crystalline surface disfavors ice nucleation.[41] Moreover, surface fluctuations in soft organic surfaces could increase their curvature or roughness,

Received: November 27, 2016
Published: January 30, 2017

DOI: 10.1021/jacs.6b12210
J. Am. Chem. Soc. 2017, 139, 3052−3064

and both were shown to decrease the freezing efficiency of model surfaces.[42,43] The second goal of this work is to determine whether fluctuations in the hydroxylated organic surfaces can, under some circumstances, result in an increase of the heterogeneous ice nucleation temperature.

It has been proposed that alcohol monolayers may induce ice-like ordering of interfacial water before the crystallization of ice.[20,24,29,44] This has been supported by indirect spectroscopic evidence from sum-frequency generation (SFG) and Fourier transform infrared (FTIR) studies.[25,32] Simulation studies on AgI,[45] kaolinite surfaces,[41] and carbon surfaces[42,43,46,47] show that ordered water domains are formed before freezing of ice induced by these surfaces. Likewise, experiments evidence water ordering at mica, which nucleates ice, but not at sapphire, which does not.[48] The third goal of this work is to determine whether ordered water domains form at the alcohol monolayer interface before crystallization and, if they do, whether they promote the formation of ice.

Molecular simulations provide a powerful tool to investigate ice nucleation.[41−43,45,47,49−75] However, the study of heterogeneous ice nucleation with simulations did not emerge until the last three years, and has focused on ice formation by graphitic,[43,46,47,55,56,58] AgI,[41,45,61,76] kaolinite,[41,57,66,77] and other crystalline model surfaces.[51,59] There has not yet been any molecular simulation studies on heterogeneous nucleation of ice by organic surfaces.

In this study, we first use molecular simulations to quantify how the order and fluctuations of hydroxyl groups in soft organic surfaces impact the heterogeneous ice-nucleating temperatures. Through the analysis of simulations of ice nucleation by alcohol monolayers, we build a master curve that represents the freezing efficiencies, defined as the difference between the heterogeneous and homogeneous ice nucleation temperatures $\Delta T_f = T_{het} - T_{hom}$, as a function of the structural matching of the surface to the basal plane of ice and the magnitude of its fluctuations. We then use the master curve to predict the freezing efficiencies for monolayers of *n*-alkyl alcohols and fatty acids using experimental structure and fluctuations data and compare the predictions with experimental results reported in the literature as well as laboratory measurements performed in this study. This study provides a perspective on how the structure of surfaces impacts the ordering of interfacial water and modulates ice nucleation temperatures and provides a framework to interpret ice nucleation temperatures in terms of the free energy of binding of ice to the nucleating surface.

2. METHODS

2.1. Molecular Simulations. Molecular dynamics simulations of alcohol monolayers in contact with water are performed with LAMMPS.[78] The equations of motion are integrated with the velocity Verlet algorithm using a time step of 5 fs and periodic boundary conditions. The temperature is controlled with the Nose-Hoover thermostat[79,80] with time constant of 5 ps. Water is modeled with the monatomic water model mW.[81] This model has been widely validated for the study of the structure, thermodynamics, and crystallization of water.[42,47,49−56,58,59,75,81−115] The equilibrium melting of mW water is $T_m = 273 \pm 0.5$ K.[109] The homogeneous ice nucleation temperature at a cooling rate of 1 K ns^{-1} is $T_{hom} = 202 \pm 2$ K.[49] The *n*-alkyl alcohol molecules are represented at the united atom level, modeling the CH_3 and CH_2 groups with the Lennard-Jones interactions of the UA-OPLS[116] force field, the hydroxyl group with mW, and using the bonds, angles, and dihedral parameters of ref 117. We assign the same bonded parameters to all sites in the alcohol molecule. The interaction between OPLS carbon types and mW hydroxyl groups is modeled through Lennard-Jones interactions with $\varepsilon_{wc} = 0.118$ kcal mol^{-1} and $\sigma_{wc} = 0.3905$ nm, the same as those for CH_2-CH_2 interactions in UA-OPLS. The interaction between OPLS carbon types and mW water is described by a Lennard-Jones potential with $\varepsilon_{wc} = 0.17$ kcal mol^{-1} and $\sigma_{wc} = 0.3536$ nm, parametrized in a previous study to reproduce the surface tension of the nonane−water interface.[117] The interaction between hydroxyl groups and water is the same as that between water molecules. To validate the model, we built monolayers with 450 molecules of the linear alcohols with either 30 or 31 carbons ($C_{30}OH$ and $C_{31}OH$) in contact with a water slab containing 13 050 molecules (the carbon tails and a side of the water slab are in contact with vacuum). We define t and δ as the tilt angles of the alcohols with respect to the normal to the monolayer−water interface in the direction of the a_{ML} and b_{ML} vectors of Figure 1, following ref 33. The

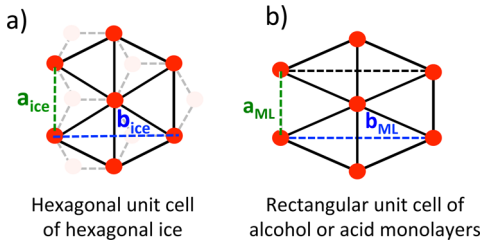

Figure 1. (a) Hexagonal unit cell showing the water bilayer in an exposed basal plane of ice. Red circles represent undercoordinated waters at the ice surface, and pink circles represent the four-coordinated layer of water molecules beneath this layer. (b) Rectangular unit cell of the lattice hydroxyl groups in alcohol monolayer, with a_{ML} and b_{ML} lattice parameters. Solid red circles represent hydroxyl groups of the alcohol monolayer. Note that to complete an ice-like bilayer the water molecules have to intercalate between the hydroxyl groups of the monolayer to play the role of the pink colored sites in the ice surface. The intercalated water molecules are the ones that bind to the ice crystal.

area per alcohol molecule and tilt of the carbon chain in the simulations at zero lateral pressure are in good agreement with the experimental values: The area per alcohol is 0.188 nm^2 in the simulations versus 0.187 nm^2 in the experiments[33] for $C_{30}OH$ and 0.186 nm^2 versus 0. 0.188 nm^2 for $C_{31}OH$.[33] The tilt angles for the $C_{30}OH$ monolayer are $t = 7.9°$ and $\delta = 3.5°$ in the simulations vs $t = 7.7°$ and $\delta = 1.7°$ in the experiments,[33] and for $C_{31}OH$, they are are $t = 8.2°$ and $\delta = 1.8°$ in the simulations versus $t = 9.7°$ and $\delta = 1.7°$ in the experiments.[33]

We perform molecular dynamics simulations of ice crystallization in the presence of monolayers of $C_{30}OH$ and $C_{31}OH$. We construct periodic simulation boxes that contain a slab of 13 050 water molecules in contact with vacuum on one side and with the hydroxyl end of a monolayer with 450 alcohol molecules (a rectangular box with 15 × 30 molecules) on the other side. The ends of the alkyl chains of the alcohols are also exposed to vacuum. Each simulation box is equilibrated for 1 ns at 280 K in the *NVT* ensemble before undergoing cooling at constant volume (allowing expansion of water against the vacuum as it is cooled) with a rate of 1 K ns^{-1} until ice crystallization is detected using the CHILL+ algorithm,[94] which we also use to distinguish cubic and hexagonal ice polymorphs. The temperature at which ice forms in the cooling ramp defines the freezing temperature T_{het} in the simulation. Error bars are computed as standard deviations from five independent repetitions of the cooling procedure for each simulation condition. The lattice mismatch between ice and the hydroxyl groups in the monolayer is computed with respect to the lattice parameters of ice in the mW model when analyzing its effect on freezing in simulations and with respect to the experimental lattice constants of ice when correlating with the experimental freezing temperatures. To measure the freezing temperature for flat rigid monolayers with different lattice mismatch, we fix the positions of the alcohols to produce the desired lattice mismatch between their

DOI: 10.1021/jacs.6b12210
J. Am. Chem. Soc. 2017, 139, 3052−3064

hydroxyl groups and the basal plane of mW ice. To determine the freezing temperature as a function of the extent of fluctuations in the monolayers, we select rigid monolayers with various lattice mismatches to ice and let the hydroxyl groups fluctuate either in the plane of the surface (in-plane fluctuations) or perpendicular to it (out-of-plane fluctuations) by constraining the motion through an external harmonic potential. The harmonic constants for in-plane and out-of-plane fluctuations range from 0.01 to 100 kcal mol^{-1} $Å^{-2}$ and from 0.001 to 50 kcal mol^{-1} $Å^{-2}$, respectively. The extent of out-of-plane fluctuations is defined as the standard deviation of the hydroxyl group distance from their average positions. The extent of in-plane fluctuations is defined as the standard deviation of the hydroxyl group distance from its four nearest hydroxyl neighbors. We compute the magnitudes of the out-of-plane and in-plane fluctuations, σ_{out} and σ_{in}, as averages over 1 ns simulations at 280 K, close to the 278 K at which the experimental fluctuations were computed for alcohol monolayers by fitting grazing X-ray diffraction data.[27]

We perform fully flexible simulations of $C_{30}OH$ monolayers with same lattice mismatches observed experimentally for $C_{16}OH$, $C_{22}OH$, and $C_{30}OH$ monolayers. We use the carbon−carbon size parameter σ_{cc} = 0.3905 nm when modeling the mismatches corresponding to $C_{16}OH$ and $C_{22}OH$, and we scale σ_{cc} to 0.3800 nm for $C_{30}OH$ to avoid inducing a static curvature to the monolayer. We then calculate the magnitude of both in-plane and out-of-plane fluctuations for each monolayer.

We define the area mismatch between the hydroxyl groups in the ice-nucleating surface and the basal plane of ice as $X_{area} = ((a_{ML} \times b_{ML})/(a_{ice} \times b_{ice}) - 1) \times 100\%$, where a_{ML} and b_{ML} are the lattice parameters corresponding to the hydroxyl groups in the ice-nucleating surface, and a_{ice} and b_{ice} are the lattice parameters for a single layer in the basal plane of ice (Figure 1). In a hexagonal lattice, $a/b = \sqrt{3}$. The mismatch between ice and the nucleating surfaces is generally different in the two surface directions. We quantify the deviation from perfect hexagonal order through the anisotropy factor $X_{aniso} = b_{ML}/(\sqrt{3}a_{ML})$.

We define as intercalated waters those that are within 3.5 Å of the hydroxyl groups of the monolayers (i.e., directly hydrogen bonded to them). We map the topography of the surface of intercalated water with the function QuickSurf[118] of Visual Molecular Dynamics (VMD).[119] QuickSurf "computes an isosurface extracted from a volumetric Gaussian density map computed from atoms or particles in the neighborhood of each lattice point".[120] We use the default parameters: radius scale = 1.0 Å, density isovalue = 0.5, and grid spacing of 1.0 Å, to build the surface. We refer the readers to the VMD manual[120] for an explanation of the algorithm and parameters.

2.2. Laboratory Measurements. We perform laboratory measurements of the freezing temperature of ice on monolayers of docosanol ($C_{22}OH$).[33] Water droplets of 0.3−5 μL are deposited on a hydrophobic substrate, and the alcohol is added to the droplet using a $CHCl_3$ spreading solvent. In each experiment, we deposit 2−3 droplets without surfactant to act as a "blank" and indicate the freezing temperature of droplets due to impurities in the water or possible defects on the hydrophobic substrate. In all cases, the droplets covered with docosanol monolayers freeze at temperatures significantly warmer (approximately 15 °C warmer) than the those of the droplets without monolayers (i.e., "blanks"), indicating that freezing is caused by the docosanol monolayers rather than impurities in the water or possible defects on the hydrophobic substrate. After evaporation of the $CHCl_3$, the monolayer coverage is calculated using the droplet size and surfactant concentration. The droplets are then placed in a temperature- and humidity-controlled flow cell that is coupled to an optical microscope.[121] The sample is cooled at a rate of 5 °C min^{-1} until all droplets are frozen. We determine the freezing temperature of each droplet with a video recorded during the cooling ramp. The freezing temperature of ice on $C_{22}OH$ monolayer is measured with monolayer coverage of 1.6.

The method discussed above is also used to investigate heterogeneous freezing by $C_{16}OOH$ (palmitic acid) monolayers. In these experiments, the freezing temperature of the uncoated droplets is the same (i.e., within experimental uncertainty) as that of the droplets coated with $C_{16}OOH$ monolayers, indicating that the freezing ability of the $C_{16}OOH$ monolayers is no better than that of the impurities of the uncoated droplets. To further constrain the freezing properties of $C_{16}OOH$ monolayers, we carry out a series of experiments with smaller droplets condensed from the vapor phase to reduce impurities in the droplets. In these experiments, solid particles of carboxylic acid crystals are first deposited onto a hydrophobic substrate. The hydrophobic substrate is then located within a flow cell with temperature and relative humidity control.[122] Next, ∼0.1 to ∼0.4 nL water droplets are condensed on the carboxylic acid crystals. We assume that palmitic acid spreads on the water droplets to form a monolayer. The freezing temperature of water droplets containing or in contact with palmitic acid particles and its monolayer is then determined using optical microscopy.

2.3. Determination of the Relation between the Binding Free Energies and Heterogeneous Nucleation Temperature. Here we explain how do we use classical nucleation theory (CNT)[123] to derive curves that predict the heterogeneous nucleation temperature T_{het} from knowledge of the binding free energy of the ice nucleus to the nucleating surface ΔG_{bind}, defined as

$$\Delta G_{bind} = \Delta\gamma - \gamma_{ice-water} \quad (1)$$

where $\Delta\gamma = \gamma_{ice-surface} - \gamma_{water-surface}$ is the difference between the surface free energy of the ice−surface and water−surface interfaces, and $\gamma_{ice-water}$ is the surface free energy of the ice−water interface. ΔG_{bind} is truly a binding free energy density, which we report per mole of ice nuclei (it has units of kJ mol^{-1} nm^2); however, we call it the binding free energy throughout this study.

To derive the relation we assume that the rate of nucleation J is the same for homogeneous and heterogeneous nucleation of ice if the droplet size (or simulation cell size) and waiting time (or cooling rate) are the same for the homogeneous and heterogeneous experiments (simulations), i.e., $J_{hom}(T_{hom}) = J_{het}(T_{het})$. The nucleation rates are computed with CNT[123]

$$J(T) = A(T) \exp(-\Delta G^*(T)/k_B T) \quad (2)$$

where the prefactor $A(T)$ is computed using the expressions of eq 1 in ref 124 for water, and of eq 4 in ref 105 for the mW model. $A(T)$ depends mostly on the diffusion coefficient of the liquid, $D(T)$, obtained from ref 124 for water and from ref 81 for the mW model. The key difference between homogeneous and heterogeneous nucleation is the expression for the nucleation barrier $\Delta G^*(T)$. The homogeneous nucleation barrier in CNT depends on the difference in chemical potential between hexagonal ice and liquid, $\Delta\mu(T)$, which for water we take from the analytical expression provided in ref 2 and for the mW model from refs 49 and 125 the density of ice $\rho(T)$ that for water we take from ref 124 and for mW we take from ref 81, and the surface tension of the ice−liquid interface $\gamma_{ice-water}(T)$:

$$\Delta G^*_{hom}(T) = 16\pi\, \gamma_{ice-water}(T)^3/(3\rho(T)^2\, \Delta\mu(T)^2) \quad (3)$$

$\gamma_{ice-water}(T)$ has not been measured directly for supercooled water in experiments or simulations. We approximate it through Turnbull's heuristic relation, $\gamma_{ice-water}(T)/\gamma_{ice-water}(T_m) = \Delta H_m(T)/\Delta H_m(T_m)$,[126] where ΔH_m is the excess enthalpy of the liquid with respect to ice and T_m is the equilibrium melting point of ice. This relationship has been shown to be a good approximation for mW water[87,115] and experiments,[127] and it was recently used to parametrize the experimental homogeneous ice nucleation rates.[124] Instead of using $\gamma_{ice-water}(T_m)$, for which a wide range of values have been reported in experiments (33 ± 3[128] and 29.1 ± 0.8)[129] and for mW water (35 ± 2,[130] 36,[131] 35 ± 1,[132] and 35.2 ± 2.5),[133] we follow the procedure of ref 124 and use J_{hom}(236 K) in the experiments and J_{hom}(240 K) in the mW simulations to infer $\gamma_{ice-surface}$ that match the corresponding experimental[124] or simulation[105] homogeneous nucleation rate at those temperatures and then use $\Delta H_m(T)$ for water[124] and mW[49] to scale the ice−liquid surface tensions. This procedure yields $\gamma_{ice-water}(T_m)$ = 31.2 mJ m^{-2} for water and $\gamma_{ice-water}(T_m)$ = 30.8 mJ m^{-2} for the mW water model. The lower value predicted through CNT at T_m compared to those directly measured at T_m probably

DOI: 10.1021/jacs.6b12210
J. Am. Chem. Soc. 2017, 139, 3052−3064

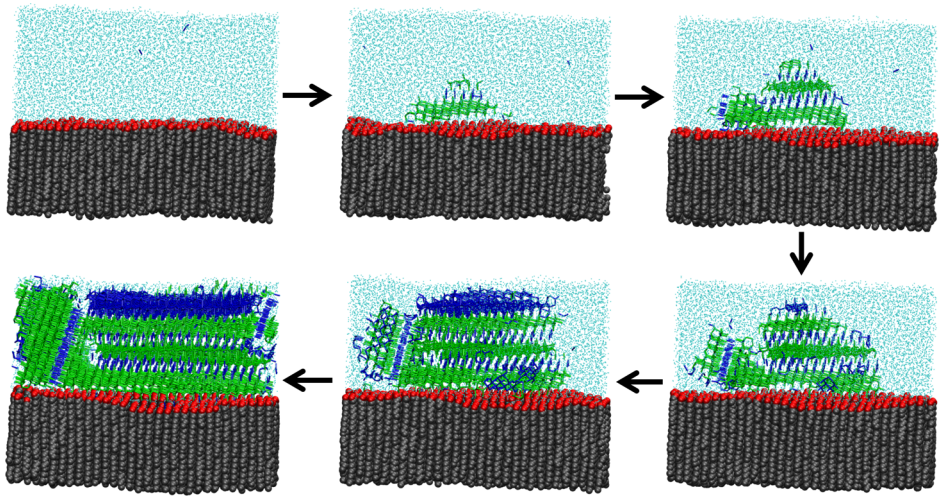

Figure 2. Snapshots along a simulation of heterogeneous nucleation of ice in the presence of a fully flexible $C_{30}OH$ alcohol monolayer. The monolayer has the area mismatch to ice of the $C_{30}OH$ monolayer in experiments (5.7% in area and 0.87 anisotropy factor[33]). The blue and green bonds indicate water with the order of hexagonal and cubic ice, respectively. Liquid water is shown with cyan points, hydroxyl groups are shown with red balls, and carbon chains are shown with gray balls. The ice nucleus that triggers the crystallization is stacking disordered, as well as the ice that grows from it.

reflects on the failure of the approximation than the critical ice nucleus is hexagonal instead of stacking disordered.[134]

The heterogeneous ice nucleation barrier ΔG^*_{het} depends on $\Delta\mu$ and $\Delta\gamma$, as well as the size and geometry of the critical nucleus (number of molecules N^*_{het}, the ice−water area $A^*_{ice-water}$, and the ice−surface area $A^*_{surface}$):

$$\Delta G^*_{het}(T) = N^*_{het}(T)\,\Delta\mu(T) + A^*_{ice-water}(T)\,\gamma_{ice-water}(T) + A^*_{surface}(T)\,\Delta\gamma(T) \quad (4)$$

N^*_{het} is related to the size of the critical nucleus for homogeneous nucleation at the same temperature by the potency factor f,[56]

$$N^*_{het}(T_{het}) = f\,N^*_{hom}(T_{het}) \quad (5)$$

where $f = (1 - \cos\theta)^2(2 + \cos\theta)/4$, and the contact angle θ between the nucleus and the surface is set by the value of $\Delta\gamma$ through Young's equation, $\gamma_{ice-water}\cos\theta + \Delta\gamma = 0$.[135] The size of the nucleus for homogeneous nucleation is given by

$$N^*_{hom}(T) = 32\pi\,\gamma_{ice-water}(T)^3/(3\rho(T)^2\,\Delta\mu(T)^3) \quad (6)$$

$A^*_{ice-water}$ and $A^*_{surface}$ are set by the geometry of the nucleus, which we compute using Young's equation. This formulation of CNT assumes the shape of the nucleus is a spherical cap. In eq 4 we neglect the contribution of the line tension τl^* to the nucleation barrier, where l^* is the critical length and τ the line tension of the ice-liquid-surface three-phase interface (τ is surface-specific and typically very small, on the order the order of 1 pN m^{-1}). This approximation should fail on approaching the complete wetting by ice limit, $\Delta G_{bind} = -2\gamma_{ice-liquid}$, as discussed in section 3.3.

With the considerations above, we find the relation between binding free energy and heterogeneous nucleation temperature for the iso-rate condition. We start by selecting a reference T_{hom}, which sets the nucleation rate $J_{hom}(T_{hom})$ through eqs 2 and 3. With this, we know $J_{het}(T_{het}) = J_{hom}(T_{hom})$, but we still need to determine T_{het} that satisfies this condition. As T_{het} depends on ΔG_{bind} through $\Delta\gamma$, and these in turn depend on temperature (see above), we implement the following algorithm to find ΔG_{bind} that corresponds to a given T_{het} for a given fixed rate. First, we make a list of values of T_{het} from T_{hom} to T_m. For each of these values of T_{het}, we straightforwardly evaluate the prefactor $A(T_{het})$ from the diffusion coefficient and determine the barrier $\Delta G^*_{het}(T_{het})$ that satisfies the iso-rate condition. Second, to find the binding free energy that corresponds to the nucleation barrier $\Delta G^*_{het}(T_{het})$ determined in the previous step, we scan all values of ΔG_{bind} spanning from 0 to $-2\gamma_{ice-liquid}$ (i.e., from no stabilization of the nucleus by the surface to the complete wetting by ice limit), and for each proposed ΔG_{bind}, we compute $\Delta G^*_{het}(T_{het})$ using eqs 4−6 until we obtain a match with the one computed in the previous step from the rate. This procedure is repeated for all values of T_{het} to make a curve $\Delta G_{bind}(T_{het})$ that corresponds to a specific iso-rate condition determined by the choice of T_{hom}.

3. RESULTS AND DISCUSSION

3.1. Surface Fluctuations Decrease Its Ice-Freezing Efficiency. We start by investigating through molecular simulations the crystallization of water in the presence of a fully flexible monolayer of triacontanol ($C_{30}OH$) with the same lattice mismatch to mW ice than the experimental triacontanol monolayer has to ice in experiments:[33] X_{area} = 5.7% and X_{aniso} = 0.87. The monolayer displays significant fluctuations that result in a dynamic, wavy interface (Figure 2). We find that ice nucleates exclusively at the surface of the monolayer, at ΔT_f = 14 ± 2 K above the temperature of homogeneous nucleation. The resulting ice is stacking disordered, in agreement with previous experiments[82] and simulations[42] of heterogeneous nucleation. The stacking plane of the ice nuclei is consistently parallel to the surface, indicating that the monolayer stabilizes the basal plane of ice. Despite the 5.7% area mismatch, the first layer of the ice nucleus is directly hydrogen-bonded to the alcohol molecules through the intercalated water molecules. These results indicate that in agreement with what was proposed in the literature[25,33] the hydroxyl groups in the monolayer template the nucleation of ice. To our knowledge, this is the first report of molecular simulations of heterogeneous nucleation of ice by an organic surface.

To understand how the intercalated water and ice accommodate the lattice mismatch and how the structure of the intercalated water and ice depend on the flexibility of the surface, we perform simulations of ice crystallization in the presence of the $C_{30}OH$ monolayers with X_{area} = 5.7% and X_{aniso} = 0.87 and three different degrees of flexibility: (i) OH fixed at the experimental crystallographic positions, (ii) flexible to fluctuate only out-of-plane, and (iii) fully flexible. Figure 3 shows snapshots of the hydroxyl groups of the monolayer and

DOI: 10.1021/jacs.6b12210
J. Am. Chem. Soc. 2017, 139, 3052−3064

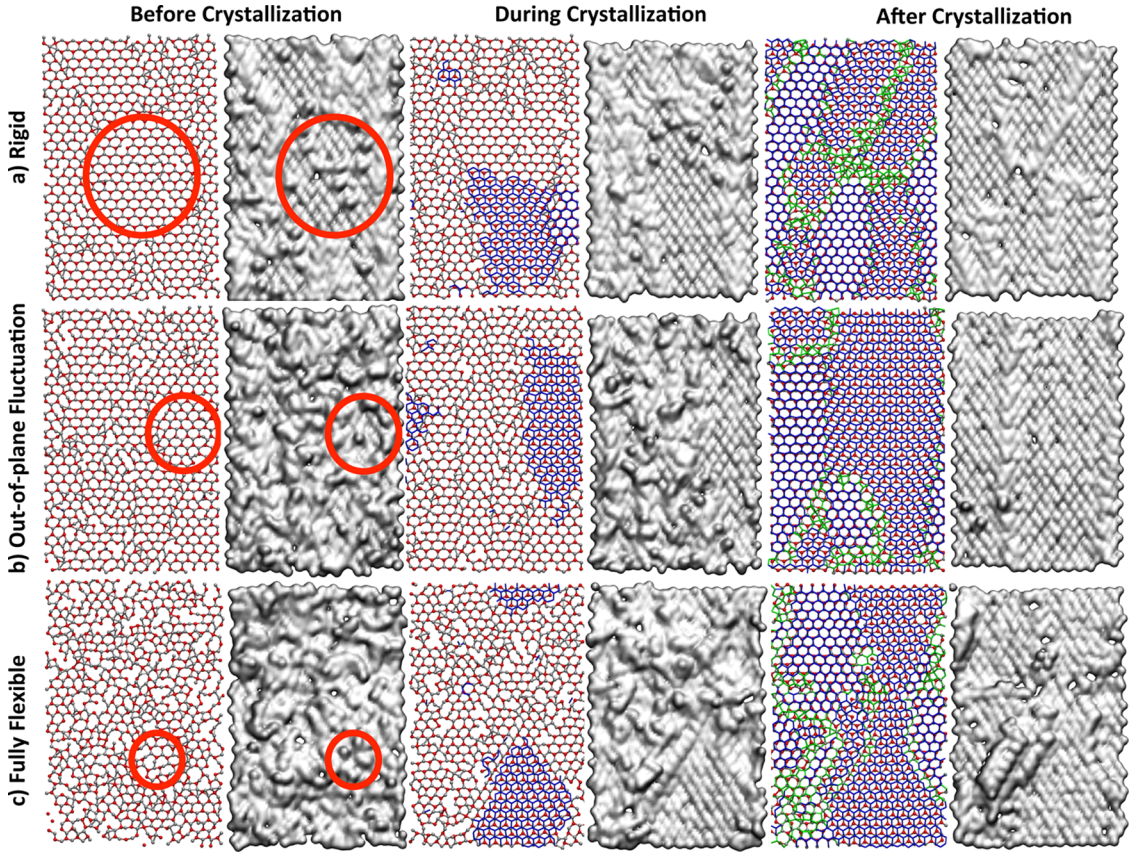

Figure 3. Snapshots of the surface of the alcohol monolayer and interfacial water along cooling simulations for (a) rigid $C_{30}OH$ monolayer, (b) $C_{30}OH$ monolayer with only out-of-plane fluctuations with σ_{out} = 1.03 Å, and (c) $C_{30}OH$ monolayer with out-of-plane fluctuations with σ_{out} = 1.46 Å and in-plane fluctuation with σ_{in} = 0.59 Å. The monolayer is 10.4% extended in the lateral direction and −4.3% contracted in the vertical direction with respect to mW ice, resulting in identical mismatch in area and anisotropy as the one between $C_{30}OH$ monolayer and ice in experiments.[33] In the static monolayer, this results in patterns of defects that are for the most part vertically aligned. Snapshots for each simulation are shown at 240 K before crystallization (left panels), during crystallization at the corresponding T_{het}, (middle panels) and after crystallization, a few degrees below T_{het} (right panels). Before crystallization, the hydroxyl groups (red balls) and the intercalated water (gray balls) complete an ice-like bilayer. As the interfacial water crystallizes, we show with blue bonds the first layer of ice, which binds directly to the intercalated water. Green bonds show, after crystallization, water in the second layer that is located between the ice domains. For each configuration, we show on the right the topography of the surface formed by the intercalated water (gray surfaces). Red circles mark the largest ordered domain formed by hydroxyls and intercalated water before crystallization.

the intercalated water under these three conditions. When liquid water is in contact with the monolayer, the water molecules closest to the surface intercalate between the hydroxyl groups of the alcohols to form the six-membered chair rings characteristic of ice (left panels of Figure 3). Together with the hydroxyl groups of the alcohol, the intercalated water molecules complete an ice-like bilayer (Figure 1). Our results render support to previous conjectures and inferences of ice-like ordering of water in contact with ice-nucleating alcohol monolayers.[20,24,25,29,30,32,44] The rings formed by the hydroxyl group of the alcohols and the intercalated waters are distorted to adapt to the underlying alcohol lattice. In the rigid monolayer, the distortion is relieved through narrow lines of defects that separate ordered domains of ice-like order. The lines of defects are very dynamic, created and annihilated within nanosecond time scales, and protrude over the plane of the hydroxyl groups, creating wrinkles in the topography of the intercalated water (gray surfaces in Figure 3). ΔT_f decreases from 33 ± 2 K for the rigid flat monolayer to 14 ± 2 K for the fully flexible monolayer. We find that an increase in the flexibility of the monolayer results in a more wrinkled topography of intercalated water, smaller ordered domains, and a depressed freezing efficiency. Our results indicate that fluctuations disfavor the formation of large ice-like ordered domains and hinder ice nucleation.

3.2. Deconstruction of the Effect of Lattice Mismatch and Fluctuations on the Ice-Freezing Efficiency. In this section, we compute the lattice mismatch and fluctuations of the hydroxylated surface exposed to liquid water and quantify their individual influence on the freezing efficiency ΔT_f. We will show that the freezing efficiency ΔT_f of the alcohol monolayers can be expressed as the product of the effect of lattice mismatch and fluctuations:

$$\Delta T_f = \Delta T_{lattice}(X_{area}, X_{aniso}) \times S_{fluct}(\sigma_{in}, \sigma_{out}) \quad (7)$$

where $\Delta T_{lattice}(X_{area}, X_{aniso})$ is the freezing efficiency of the rigid, flat surface with area mismatch to ice given by X_{area} and anisotropy X_{aniso} (see section 2.1), and $S_{fluct}(\sigma_{in},\sigma_{out})$ is the scaling factor that quantifies the impact of in-plane fluctuations with magnitude σ_{in} and out-of-plane fluctuations with magnitude σ_{out} on the ice-freezing efficiency. In the following sections, we address each of these terms and their impact on ΔT_f.

DOI: 10.1021/jacs.6b12210
J. Am. Chem. Soc. 2017, 139, 3052−3064

Experiments have shown that the shorter the alcohol chain the less compact the monolayer[33] and the lower its freezing efficiency.[24,27,28,33] Our analysis shows that increasing the area mismatch X_{area} in perfectly hexagonal flat rigid monolayers (i.e., $X_{aniso} = 1$, $\sigma_{in} = \sigma_{out} = 0$) results in a decrease in the freezing temperature T_{area} (Figure 4a). The depression of the crystallization temperature correlates with a decreasing size of domains of ordered hexagons formed by the hydroxyl groups of the alcohols and the intercalated water molecules from the liquid phase (Figure 5a–c). When X_{area} reaches 19%, ice nucleation becomes homogeneous: $T_{area} = T_{hom} = 202$ K for the mW water model at the cooling rate of 1 K ns^{-1} we use to determine the freezing temperatures. The shortest alcohol for which experimental ice-freezing temperature is available, $C_{14}OH$,[33] has the same area mismatch ($X_{area} = 16\%$[27]) and freezing efficiency ($\Delta T_f = 9$ K[33]) as $C_{16}OH$. Monolayers of alcohols shorter than $C_{10}OH$ are no longer crystalline at room temperature,[136] and we are not aware of experimental studies showing them to have the ability to nucleate ice.

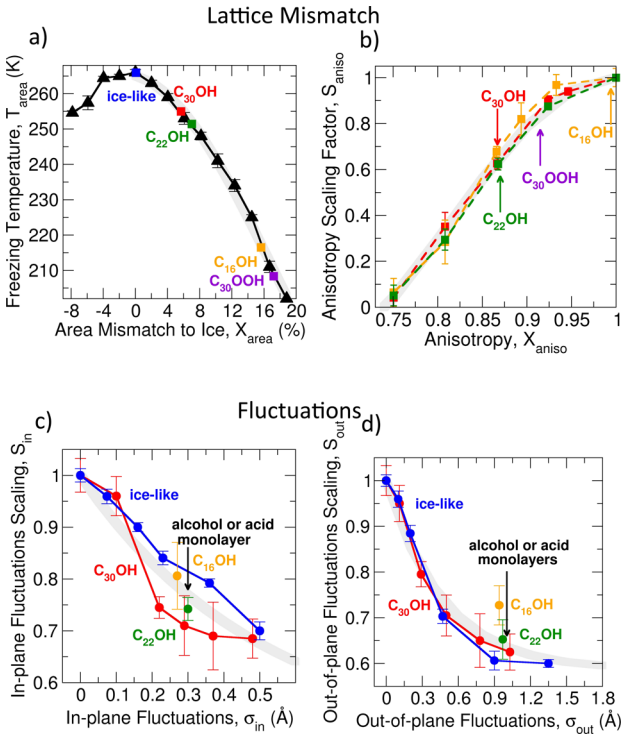

Figure 4. Effect of lattice mismatch and fluctuations on the ice-freezing efficiency of alcohol monolayers. (a) Heterogeneous freezing temperature T_{area} of alcohol monolayers in simulations of rigid monolayers without anisotropy (i.e., $\sigma_{in} = \sigma_{out} = 0$ and $X_{aniso} = 1$) as a function of area mismatch X_{area} to mW ice, determined at a nucleation rate for which $T_{hom} = 202$ K.[49] Purple, orange, green, and red squares indicate the X_{area} of alcohols and acid monolayers: 17.0% ($C_{30}OOH$), 15.5% ($C_{16}OH$), 6.6% ($C_{22}OH$), and 5.7% ($C_{30}OH$), respectively. The highest freezing temperature, 266 K, occurs when there is no mismatch to ice, $X_{area} = 0$ (blue square). The gray line represents the fit of T_{area} as a function of X_{area}, $T_{area} = 63.41 \times \sin(0.16\sqrt{X_{area} + 1} + 1.52)$. (b) Anisotropy scaling factor, S_{aniso} as a function of the lattice anisotropy, X_{aniso}. The orange, green, and red squares correspond to monolayers with the area mismatch of $C_{16}OH$, $C_{22}OH$ and $C_{30}OH$, respectively. The values of X_{aniso} for these alcohols and the $C_{30}OOH$ acid are indicated with arrows: 1.0 for $C_{16}OH$, 0.87 for $C_{22}OH$, 0.87 for $C_{30}OH$, and 0.90 for $C_{30}OOH$. S_{aniso} reaches zero when X_{aniso} approaches 0.75. The gray line represents the best fit, which is independent of X_{area}, $S_{aniso} = 0.64 \sin(8.41X_{aniso} - 6.84) + 0.36$. (c) Scaling factor of the freezing efficiency S_{out} due to out-of-plane fluctuations σ_{out}. Orange, green and red circles show S_{out} for simulations with X_{area} and X_{aniso} of $C_{16}OH$, $C_{22}OH$ and $C_{30}OH$, respectively; blue circles show S_{out} for a monolayer of perfect ice-like order, $X_{area} = 0$ and $X_{aniso} = 1$. The black arrow indicates the experimental σ_{out} for alcohol and acid monolayers. Gray curve is the best fit to these measured points, $S_{out} = 0.41e^{(-2.11\sigma_{out})} + 0.59$. (d) Scaling factor S_{in} of the freezing efficiency due to in-plane fluctuations σ_{in}. Coloring as in panel c. Experimental σ_{in} for monolayers are pointed out with arrows in black. The gray curve represents the best fit, $S_{in} = 0.52e^{(-1.96\sigma_{in})} + 0.48$.

The ice-freezing temperature decreases as the arrangement of hydroxyl groups in the nucleating surface departs from perfectly hexagonal (Figure 4b). We define the anisotropy scaling factor as the fractional decrease in freezing efficiency when the lattice is distorted keeping the area constant, $S_{aniso} = \Delta T_{lattice}(X_{area}, X_{aniso})/\Delta T_{lattice}(X_{area}, 1) = \Delta T_{lattice}(X_{area}, X_{aniso})/\Delta T_{area}(X_{area})$, where ΔT_{area} is the freezing efficiency of the perfectly hexagonal rigid surface, $T_{area} - T_{hom}$. We find that S_{aniso} is independent of the area mismatch (Figure 4b). This implies that the total contribution of the area and anisotropy mismatch to the freezing efficiency can be written as a product of two independent contributions, $\Delta T_{lattice}(X_{area}, X_{aniso}) = \Delta T_{area}(X_{area}) \times S_{aniso}(X_{aniso})$. Figure 5b,c,e,f shows that, as previously discussed for the area mismatch, the decrease in T_{het} with increasing anisotropy of the ordering of hydroxyl groups in the surface is associated with diminishing size of the domains of ordered hexagons formed by the hydroxyl groups of the alcohols and the intercalated water molecules from the liquid phase.

The monolayers of Figure 3 have identical area and anisotropy, but different freezing temperatures. This implies that knowledge of the lattice mismatch is insufficient to predict the freezing temperature; fluctuations of the templating surface must also be considered. We find that in-plane and out-of-plane fluctuations always decrease the freezing efficiency (Figure 4c,d). It has been conjectured that fluctuations could compensate for the in-plane lattice mismatch in alcohol monolayers and assist in the nucleation of ice.[25,40] That would require coherence of in-plane fluctuations to form domains with ice-like order and matching. Figure 3 shows that fluctuations have the opposite effect, diminishing the size of the ice-like templating domains.

We interpret that out-of-plane fluctuations hinder nucleation because they increase either the curvature or roughness of the surface, and both have been shown to decrease the crystallization temperature of ice.[42,43] We note that the experimental σ_{out} was measured by grazing X-ray diffraction with wavelength of ~30 nm[27] while σ_{out} in our simulations is measured from periodic cells with dimensions ~10 nm. This suggests that the local curvature corresponding to a given value of σ_{out} could be larger in the simulations and result in a stronger depression of the freezing efficiency compared to experiment.

Figure 4c,d shows that the scaling of the freezing efficiency due both to in-plane and out-of-plane fluctuations is essentially independent of the lattice mismatch, $S_{in}(X_{area}, X_{aniso}, \sigma_{in}) = \Delta T_{in}(X_{area}, X_{aniso}, \sigma_{in})/\Delta T_{lattice}(X_{area}, X_{aniso}) = S_{in}(\sigma_{in})$ and $S_{out}(X_{area}, X_{aniso}, \sigma_{out}) = \Delta T_{out}(X_{area}, X_{aniso}, \sigma_{out})/\Delta T_{lattice}(X_{area}, X_{aniso}) = S_{out}(\sigma_{out})$. Assuming independent scaling effects of in- and out-of-plane fluctuations, the total scaling due to fluctuations is their product, $S_{fluct}(\sigma_{in}, \sigma_{out}) = S_{in}(\sigma_{in}) \times S_{out}(\sigma_{out})$. We combine the effect of lattice mismatch and fluctuations into a master curve that predicts the freezing

DOI: 10.1021/jacs.6b12210
J. Am. Chem. Soc. 2017, 139, 3052–3064

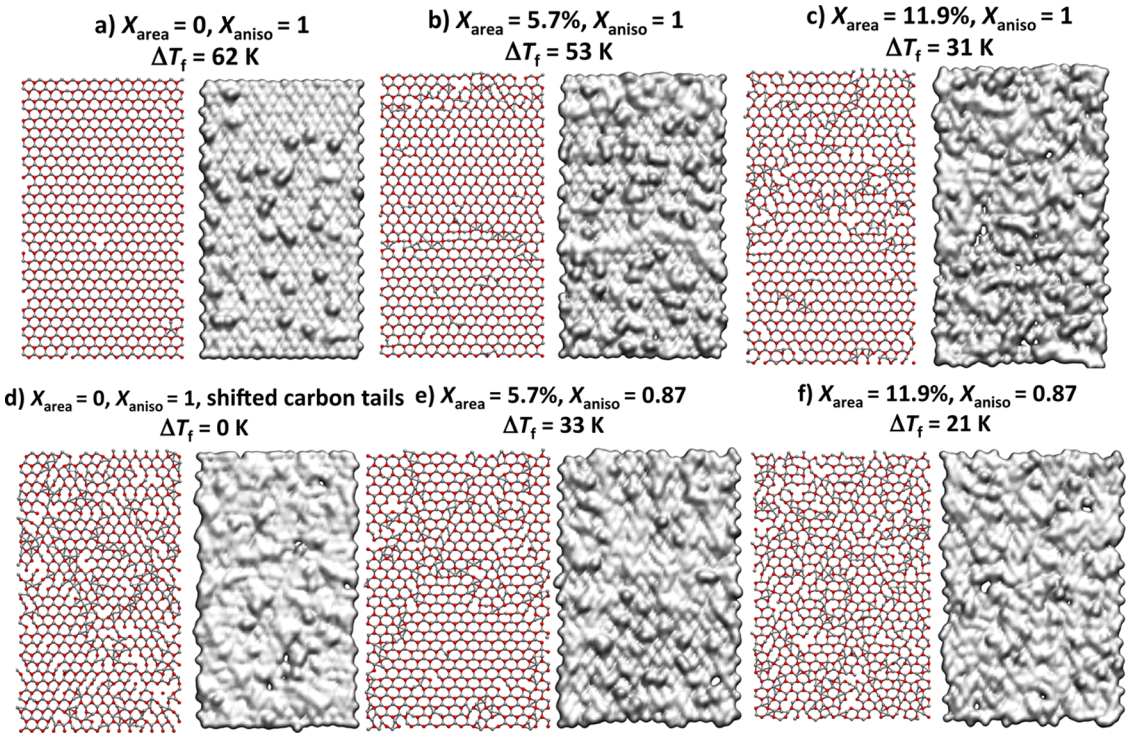

Figure 5. Increase in the roughness of intercalated water correlates with a decrease in ice-freezing efficiency. All surfaces correspond to rigid alcohol monolayers, with different lattice mismatch (a–c, e–f) or displacement of the carbon tails by half unit cell (2.215 Å in the direction of the *a* vector in Figure 1) in (d), indicated in the corresponding labels. Same representations and color coding as in Figure 3: Left panel for each surface shows the hydroxyl groups in red and intercalated water in gray; right panel shows the surface (topography) of the intercalated water at the interface. The labels indicate the freezing efficiency of each surface, which decreases with increasing roughness of the intercalated water.

Table 1. Comparison of ΔT_f in Simulations of Unconstrained Monolayers and Predictions of the Master Curve Using the Values of X_{area}, X_{aniso}, σ_{out}, and σ_{in} Obtained from the Simulations

surface	lattice mismatch, X_{area}, %	lattice anisotropy, X_{aniso}	out-of-plane fluctuations, σ_{out} (Å)	in-plane fluctuations, σ_{in} (Å)	$\Delta T_f^{master\ curve}$ (K)	$\Delta T_f^{simulation}$ (K)
$C_{30}OH$[a]	5.7	0.87	1.46	0.59	13	14 ± 2
$C_{20}OH$[a]	14.2	0.92	0.94	0.54	8	9 ± 3
$C_{16}OH$[b]	15.5	1.0	1.20	0.55	7	10 ± 2

[a]Lattice parameters from ref 33. [b]Lattice parameters from ref 27.

efficiency ΔT_f of fully flexible alcohol monolayers in terms of X_{area}, X_{aniso}, σ_{in}, and σ_{out}:

$$\Delta T_f(X_{area}, X_{aniso}, \sigma_{in}, \sigma_{out}) = \Delta T_{area}(X_{area}) \times S_{aniso}(X_{aniso}) \times S_{out}(\sigma_{in}) \times S_{in}(\sigma_{out}) \quad (8)$$

The functional forms of these four functions, the gray curves of Figure 4, are given in the caption of that figure. Table 1 shows that ΔT_f predicted by the master curve given by eq 8 for fully flexible monolayers with the experimental lattice mismatch and anisotropy[27,33] of $C_{30}OH$, $C_{22}OH$ and $C_{16}OH$ are in very good agreement with the ΔT_f measured for these monolayers in the molecular simulations. This validates the assumption that the freezing efficiency of the alcohol monolayers arises from uncoupled contributions due to area mismatch, anisotropy, in-plane fluctuations, and out-of-plane fluctuations.

Alcohols with odd carbon tails are more efficient in promoting nucleation of ice than those with even carbon tails.[24,33] It has been proposed that the effect may arise from the relative orientation of the OH bond of the alcohols with respect to the surface.[33] A recent simulation study suggests that reorientation of hydroxyl groups on rigid kaolinite surface promotes ice nucleation.[41] The lack of explicit hydrogen atoms in the coarse-grained model prevents it from capturing that effect: The ice-freezing temperatures in simulations with fully flexible monolayers of $C_{30}OH$ or $C_{31}OH$ are identical. The master curve for nucleation by hydroxylated surfaces (eq 8) was built to represent the trend in freezing efficiencies of the series of alcohol monolayers with even number of carbon atoms in their tails. We compute the ratio of the experimental freezing efficiencies of odd versus even alcohol chains, $S_{odd} = \Delta T_f(C_{n+1}OH)/\Delta T_f(C_nOH)$, from the data of ref 33 and find it to be independent of the length of the hydrocarbon chain, 1.20 ± 0.05. Since experiments demonstrate (and our simulations confirm) that lattice parameters and fluctuations of $C_{n+1}OH$ and C_nOH are almost identical for each n,[27,33] multiplication of ΔT_f of eq 8 by the S_{odd} factor could be used to extend the predictions to odd-chain alcohol monolayers.

3.3. Binding Free Energy of Ice to the Surface Controls the Freezing Efficiency. To compare the ΔT_f predicted by the master curve constructed from simulation data (eq 8) with ΔT_f measured in experiments of ice crystallization by alcohol monolayers we must take into account that the

DOI: 10.1021/jacs.6b12210
J. Am. Chem. Soc. 2017, 139, 3052–3064

crystallization rates used to obtain T_{het} are different in the simulations and experiments. We derive in section 2.3 a relationship between the binding free energy of ice to the nucleating surface ΔG_{bind} and the temperature of heterogeneous ice nucleation T_{het} using the framework of classical nucleation theory (CNT).[123] We assume that the rate of heterogeneous nucleation at T_{het} is the same as the rate of homogeneous nucleation at T_{hom}, which is an appropriate approximation if the time scales of the heterogeneous and homogeneous nucleation experiments (or simulations) are the same. The ice nucleation rate in the simulations of homogeneous and heterogeneous crystallization of this study is $\sim 10^{27}$ cm^{-3} s^{-1}, given by the cooling rate and volume of the simulation cells.[49,87] The experiments of ice nucleation by alcohol monolayers in the literature[33] and in this study are conducted at conditions that lead to T_{hom} = 238 K, which corresponds to a nucleation rate of $\sim 10^{5}$ cm^{-3} s^{-1}.[124] For each nucleation rate, we compute the freezing efficiency $\Delta T_f = T_{het} - T_{hom}$ that corresponds to the binding free energy of ice ΔG_{bind}. Figure 6 shows the relation between ΔG_{bind} and ΔT_f derived using experimental data[2,124] at the nucleation rate corresponding to T_{hom} = 238 K (orange curve) and using mW data[49,81] at the nucleation rates that produce T_{hom} = 238 and 202 K (green curves). The binding free energy must be negative to promote heterogeneous nucleation. Figure 6 shows that for a given nucleation rate the stronger the binding of ice to the surface the more stabilized is the ice nucleus and the higher the heterogeneous freezing temperature.

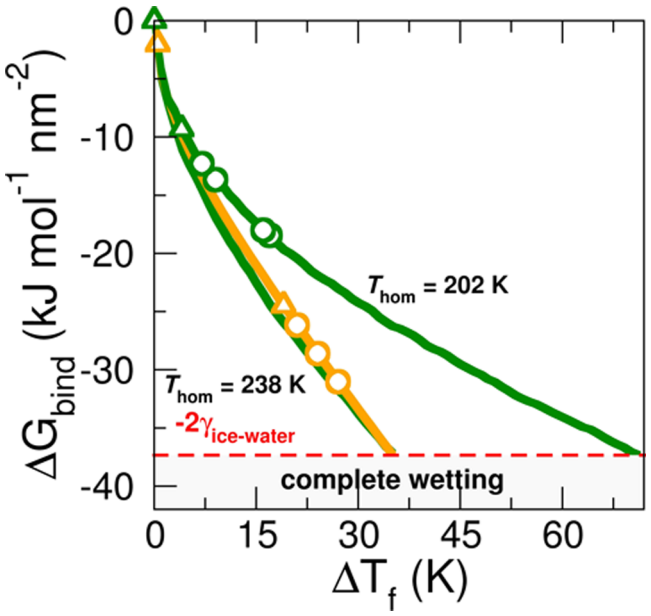

Figure 6. Relation between the binding free energy of a surface to ice, ΔG_{bind}, and its freezing efficiency ΔT_f for the CNT parametrization for mW water[49,81] (green) at the nucleation rate that produces T_{hom} = 202 K in ($J = 10^{25}$ cm^{-3} s^{-1}) and T_{hom} = 238 K ($J = 10^{-9}$ cm^{-3} s^{-1}) and for the CNT parametrization of the experimental data[2,124] (orange) at the rate that produces T_{hom} = 238 K ($J = 10^{5}$ cm^{-3} s^{-1}). The two curves end at the melting point of ice, which is indistinguishable from that of the experiment and mW water.[109] In the gray area, $\Delta G_{bind} \leq -2\gamma_{ice-water}$, the nucleus completely wets the surface, and according to CNT, the nucleation barrier vanishes if the contribution of the line tension between ice−liquid−surface is neglected. Circles indicate $\Delta G_{bind}(\Delta T_f)$ of alcohol monolayers in experiments (orange) and predicted by the master curve built from simulations (green) and triangles $\Delta G_{bind}(\Delta T_f)$ of acid monolayers in experiments (orange) and predicted by the master curve built from simulations (green).

The ice nucleus completely wets the surface when the binding free energy approaches $-2\gamma_{ice-water}$ ($\Delta G_{bind} \rightarrow -2\gamma_{ice-water}$, dashed line in Figure 6). Equation 4 predicts that the formation of the critical nucleus is barrierless beyond that limit (region of complete wetting by ice in Figure 6). On approaching this limit, the line tension of the ice−liquid−surface line, neglected in eq 4, would make an important contribution to the free energy barrier of nucleation and should be included in the CNT formulation.[137,138] Moreover, Iwamatsu has demonstrated that the existence of prewetting transitions leads to break down of CNT on approaching the complete wetting by ice limit, which results in a finite nucleation barrier for the heterogeneous nucleation of liquid from vapor.[139] The conclusions of ref 139 have not yet been generalized for the nucleation of a crystalline nucleus on a soft, wavy surface; but they would suggest that for surfaces with $\Delta G_{bind} \leq -2\gamma_{ice-water}$ the freezing temperature approaches the equilibrium melting line but a finite barrier could still exist for heterogeneous nucleation.

The prediction of the binding free energy of ice to a surface using CNT depends in principle on the properties of water or the model, but does not require specific knowledge of the chemistry of the surface; only its freezing efficiency. We note that the iso-rate curves $\Delta G_{bind}(\Delta T_f)$ for T_{hom} = 238 K built using experimental and mW data are essentially identical (Figure 6). The curve $\Delta G_{bind}(\Delta T_f)$ depends on the selected nucleation rate (i.e., on the reference T_{hom}). Figure 6 indicates that for a surface with a given ΔG_{bind} the ΔT_f is larger when the nucleation rate is faster. Hence, it would be expected that if the simulations reproduce the experimental binding free energies of the monolayers to ice, then ΔT_f predicted by the master curve parametrized from simulations with T_{hom} = 202 K should be larger than the one measured in the experiments with T_{hom} = 238 K. In what follows, we predict ΔT_f for the alcohol monolayers using the master curve of eq 8 with the experimental lattice parameters (X_{area} and X_{aniso}) and fluctuations (σ_{in} and σ_{out}) for C_nOH with n = 30, 22, 20, and 16 and compare these results with the ΔT_f measured for the same alcohol monolayers in experiments. We use experimental lattice data from refs 27, 33, and 140 and fluctuations σ_{in} = 0.3 Å and σ_{out} = 1.0 Å for alcohols with $n \geq 20$ and σ_{in} = 0.6 Å and σ_{out} = 1.0 Å for $C_{16}OH$ from ref 27. The master curve predicts $S_{fluct}(\sigma_{in}, \sigma_{out})$ to be 0.49 for monolayers of $C_{22}OH$ to $C_{30}OH$ and 0.41 for the monolayer of $C_{16}OH$. Fluctuations decrease the predicted freezing efficiency of alcohol monolayers by more than 50%. The deconstruction of the effects of lattice mismatch and fluctuations on the predicted freezing efficiency of alcohol monolayers suggests that both are important factors in determining the magnitude of ΔT_f.

The ΔT_f for the monolayer of $C_{22}OH$ is measured in this work. The experimental T_{het} of the monolayers of $C_{30}OH$, $C_{20}OH$, and $C_{16}OH$ are taken from ref 33. In previous experimental studies, the freezing point of pure water droplets ranged from 253 to 248 K.[24] This limit, however, must be due to heterogeneous nucleation by impurities in water or associated with other aspects of the experimental device, as the expected T_{hom} in these experiments should be 238 K.[141] We note that is difficult to quantify the uncertainty in T_{het} of the monolayers: Our laboratory measurement of T_f on single-component microliter droplets coated with $C_{22}OH$ monolayer results in T_f at least 5 K lower than those reported in ref 33.

DOI: 10.1021/jacs.6b12210
J. Am. Chem. Soc. 2017, 139, 3052−3064

The uncertainties could arise from variations in the coverage of the droplets, which can result in different density and ordering of the molecules in the monolayer, and even due to the presence of alcohol crystallites if the coverage exceeds the one of a single monolayer. Our analysis indicates that these changes in order would result in distinct abilities to promote water freezing.

The master curve predicts the right trend of ΔT_f across the alcohols, but underestimates by 10−15° the absolute freezing efficiency of each monolayer (Figure 7). The underestimation is

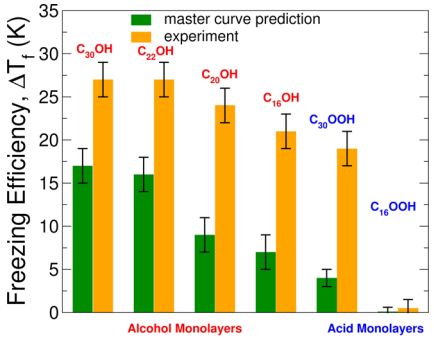

Figure 7. Freezing efficiencies ΔT_f of alcohol and acid monolayers measured in experiments with nucleation rates $J \approx 10^5$ cm^{-3} s^{-1} and predicted by the master curve (eq 8) built from simulations with nucleation rates $J \approx 10^{25}$ cm^{-3} s^{-1}. Green bars are predictions with the master curve using experimental structure and fluctuation data. Orange bars are experimental measurements for the alcohols from ref 33, for $C_{30}OOH$ from ref 33, and our own measurements for $C_{22}OH$ and $C_{16}OOH$. For palmitic acid, the monolayer is in contact with a crystal. Experimental lattice mismatch for $C_{19}OOH$ monolayer is already larger than 20% at the equilibrium surface pressure,[34] and it should be even larger for $C_{16}OOH$ monolayers, resulting in null freezing efficiency. Experimental lattice mismatch at 278 K for $C_{20}OH$ (X_{area} = 14.2% and X_{aniso} = 0.92) and $C_{30}OH$ ((X_{area} = 5.7% and X_{aniso} = 0.87) from ref 33, for $C_{22}OH$ at 283 K (X_{area} = 6.6% and X_{aniso} = 0.87) from ref 140, for $C_{16}OH$ at 278 K (X_{area} = 15.5% and X_{aniso} = 1.0) from ref 27, and for $C_{30}OOH$ at 278 K (X_{area} = 17.0% and X_{aniso} = 0.90) from ref 24.

not due to the difference in nucleation rates in the experiments and simulations, as the curves of Figure 6 predict that for a given surface (i.e., a given ΔG_{bind}) ΔT_f for the experimental nucleation rate should be the smallest. This implies that the binding free energy of ice to the alcohol monolayers is weaker than in the experiment. Indeed, Figure 8 shows that the ΔG_{bind} for each alcohol monolayer deduced from the experimental ΔT_f (orange circles in Figure 6) is larger than the corresponding one computed from the ΔT_f predicted with the master curve (green circles in Figure 6). The discrepancy may have a multitude of origins. First, as we discussed in section 3.2, the radius of curvature R_c of the surface for a given σ_{out} might be smaller in the simulations than in the experiment, because the simulation cells are smaller than the ∼30 nm wavelength with which σ_{out} was sensed in experiments.[27] Previous work on graphitic surfaces has shown that ΔT_f decreases with decreasing R_c and that the depression is particularly pronounced when R_c is comparable to the length scale of the critical nuclei.[42] The extent of this correction could be assessed through comparison of q-dependent capillary wave amplitudes in experiments and simulations. Second, the predictions of Figure 8 are based on the validity of CNT. A first assumption in our implementation of CNT is that the critical nucleus is made of hexagonal ice. It

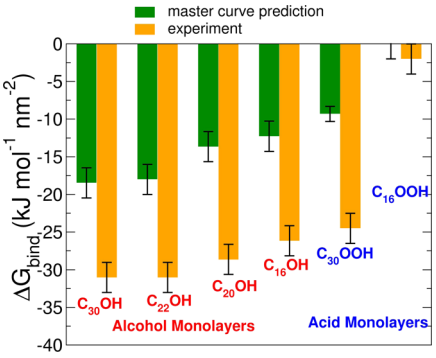

Figure 8. Binding free energy of the surface to ice, ΔG_{bind}, derived from Figures 6 and 7 for alcohol and acid monolayers. Green bars are derived from ΔT_f predicted by master curve through the iso-rate curve of ΔG_{bind} (ΔT_f) for mW water at T_{hom} = 202 K. Orange bars are derived from experimental ΔT_f through the iso-rate curve of ΔG_{bind} (ΔT_f) for water at T_{hom} = 238 K. The ΔG_{bind} for each surface deduced from experiments and master curve in Figure 6 would correspond to different temperatures. However, if the entropy of binding is small ($\Delta S_{bind} \approx 0$), then ΔG_{bind} would be almost independent of temperature.

has been shown that the ice nucleus is stacking-disordered[63,82,83,111,134,142] and that this leads to a correction to the nucleation rates that is size-dependent.[134] However, there is not yet an accurate expression for the correct $\Delta\mu$ for stacking-disordered nuclei as a function of nucleus size that we can implement in the theory, and this correction may not contribute much to the difference in predicted free energy of binding between model and experiments if the extent of stacking disorder is comparable in the two. We also assumed in the CNT derivation that the ice nucleus has the shape of a spherical cap, which has been verified for ice nucleation on carbon surfaces[46,56] but has been recently questioned for kaolinite surfaces.[72] We do not expect this to be a main source of the difference in ΔG_{bind} derived from experiments and master curve parametrized from simulations. As indicated in the Methods section, in our derivation of $\Delta G_{bind}(\Delta T_f)$ we neglect the contribution of the line tension of the ice−liquid−surface contact line to the free energy barriers. This may impact $\Delta G_{bind}(\Delta T_f)$ as T_{het} approaches T_m, but should be a good approximation far from the complete wetting by ice limit. CNT also assumes that the size of the nucleus is the reaction coordinate for heterogeneous nucleation of ice. This approximation was demonstrated to be correct for rigid carbon surfaces,[46,56] but still has to be determined whether it holds for flexible surfaces, such as alcohol monolayers. The third possible origin for the discrepancy between the binding free energies deduced from the T_{het} predicted by the master curve and those deduced from the T_{het} in the experiments may be inaccuracies in the force field. In the following, we analyze the effect of water−alcohol interaction on the freezing efficiency of the surfaces.

To understand the sensitivity of the freezing efficiency (and binding free energy) to the strength of the alcohol−water interaction, we show in Figure 9 how T_{het} is modulated by the strength of the (i) water−carbon interaction, ε_{wc}, and (ii) water−hydroxyl interaction, ε_{wOH}. We find that the ice-freezing temperature of perfectly hexagonal rigid monolayers with 0 and 6.6% area mismatch to mW ice decreases monotonically with increasing water−carbon attraction. The displacement of T_{het} with ε_{wc} seems to be independent of X_{area}. The freezing

DOI: 10.1021/jacs.6b12210
J. Am. Chem. Soc. 2017, 139, 3052−3064

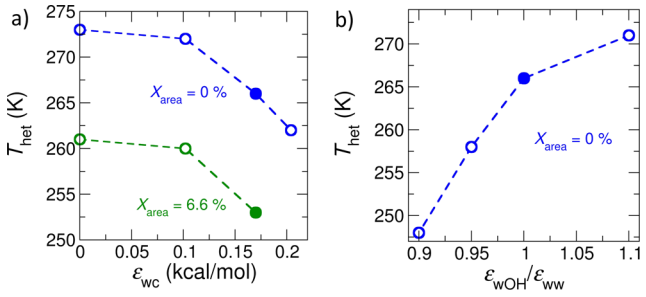

Figure 9. Sensitivity analysis of the ice-freezing temperature T_{het} to the parameters of the water−alcohol interaction potential, measured in simulations of water in contact with rigid alcohol monolayers. (a) T_{het} decreases with increasing strength of water−carbon interaction ε_{wc}. Blue circles correspond to the rigid monolayer with perfect structural matching to ice, X_{area} = 0 and X_{aniso} = 1. Green circles correspond to the monolayer with the area mismatch of the $C_{22}OH$ monolayer in experiments, X_{area} = 6.6%, but without any anisotropy, i.e., X_{aniso} = 1. Filled circles indicate the parameters in the simulations used to build the master curve. Additional calculations for various X_{aniso} at X_{area} = 0 and 6.6% indicate that S_{aniso} is insensitive to the strength of the water−carbon interactions ε_{wc}. (b) T_{het} increases with increasing ratio between the strength of OH−water interaction ε_{wOH} and water−water interaction ε_{ww}. As in panel a, blue circles represent the rigid monolayer with perfect structural matching to ice. The filled circle corresponds to the parameter used to build the master curve in this study. According to *ab initio* CCSD(T) calculations, the average strength of the optimized water−alcohol hydrogen bond is 10 and 13% higher than for water−water for methanol and ethanol, respectively.[143]

efficiency of the surface is affected not only by the strength of the water−carbon interaction but also by the position of the carbon chains with respect to the hydroxyl group of the alcohol. We find that the flat monolayer with perfect matching to ice becomes unable to nucleate ice if we displace the hydroxyl groups with respect to the tails by half unit cell (2.215 Å in the direction of the *a* vector in Figure 1). It is interesting to note that this ineffective surface lacks the ordered domains of hydroxyl groups and intercalated waters that correlate with the surface ice-freezing efficiency (Figure 5d). We conclude that the van der Waals interactions between water and the hydrocarbon tails promote an ordering of water that creates a barrier against crystallization. However, even an unphysical value of ε_{wc} = 0 would not be enough to account for the difference between the water model and experiments. Promotion of ice crystallization by the monolayers relies exclusively in templating by the hydroxyl groups.

The freezing efficiency of the surface increases with the strength of the water-hydroxyl interaction, ε_{wOH} (Figure 9b). Coupled cluster CCSD(T) calculations of optimized hydrogen-bonded water−methanol and water−ethanol complexes indicate that alcohol water hydrogen-bonds (HB) are, in average, stronger than water−water HB.[143] To complete the ice-like bilayer, each hydroxyl group should HB to three water molecules (Figures 1 and 3) through an average of one donor and two acceptor HBs. CCSD(T) predicts that the average ratio of HB energy in water−alcohol to water−water is 1.14 and 1.01 for methanol as acceptor and donor, respectively, and 1.21 and 0.97 for ethanol as acceptor and donor, respectively.[143] The averages for two donor and one acceptor HBs are $\varepsilon_{wOH}/\varepsilon_{ww}$ = 1.10 and 1.13 for optimized water−methanol and water−ethanol complexes and are not known for water binding alcohol monolayers. The coarse-grained model of this study lacks hydrogen atoms and cannot distinguish between donor and acceptor HBs. However, the model could be reparameterized with more accurate energetics for the binding of water to alcohol that would improve the prediction of binding free energies.

3.4. Fatty Acid Monolayers Have Lower Freezing Efficiency Because of Their Large Area Mismatch. Monolayers of fatty acids promote ice nucleation at temperatures lower than monolayers of alcohols with the same length of the carbon chain (see Figure 7).[33] We predict the freezing efficiency of monolayers of $C_{30}OOH$ (melissic acid) and $C_{16}OOH$ (palmitic acid) with the master curve built from the simulations of alcohols, using experimental structural data (X_{area} = 17.0%, X_{aniso} = 0.90[24] for $C_{30}OOH$, X_{area} larger than the 20% that results in homogeneous nucleation for $C_{16}OOH$, as it is already more extended for $C_{19}OOH$)[34] and fluctuations (σ_{out} = 1.0 Å,[27] σ_{in} = 0.3 Å, assuming the later to be the same as for alcohol monolayers)[27] for the acid monolayers. The master curve captures the difference in ΔT_f between $C_{30}OH$ and $C_{30}OOH$ monolayers, $\Delta(\Delta T_f)$ = 8 ± 4 K using the experimental freezing temperatures from ref 33 and 13 ± 4 from the predictions with the master curve although, similar to the alcohols, it under-predicts the absolute freezing efficiencies (Figure 7), and the corresponding binding free energies of ice to the acid monolayers (triangles in Figures 6 and 8). The freezing temperatures by carboxylic acid monolayers from ref 33 should be considered as upper limits since in these studies freezing by impurities were not ruled out. In addition, later studies using much smaller droplet volumes indicated that the freezing of nonadecanoic acid coated droplets was indistinguishable from uncoated droplets to nearly −30 °C.[34] The comparison of the structural and fluctuation contributions to ΔT_f of $C_{30}OOH$ and $C_{30}OH$ indicates that the difference in freezing efficiency is due to their different area per molecule. We conclude that the large area mismatch between ice and acid monolayers is responsible for their low ability to nucleate ice.

As for alcohols, the experimental lattice mismatch between ice and fatty acid monolayers increases on decreasing the length of the acid chain.[24] In good agreement with the results from the experiments (Figure 7), the master curve predicts that the palmitic acid monolayer, which must have lattice mismatch larger than 20% measured for the $C_{19}OOH$ monolayer at the equilibrium surface pressure,[34] results in null freezing efficiency. The freezing efficiency of palmitic acid monolayers may increase on compression, as it experiences a phase transition from extended rhombohedra to more compact hexagonal order[145−148] that decreases the mismatch to ice. The crystal of palmitic acid in contact with the monolayer have even larger area mismatch to ice: we compute X_{area} = 33% from the crystallographic data of Figure 1 of ref 144. This would make palmitic acid crystal an even less effective ice nucleant than the monolayer.

4. CONCLUSIONS

In this study we use molecular simulations and laboratory experiments to elucidate and quantify the impact of structural order and fluctuations of organic surfaces that expose hydroxyl groups to water on the temperature at which they nucleate ice. To our knowledge, this is the first molecular simulation study of ice nucleation by organic surfaces. The simulations indicate that the freezing efficiency $\Delta T_f = T_{het} - T_{hom}$ for this class of surfaces can be expressed in terms of the freezing efficiency of a flat rigid surface with the corresponding area per hydroxyl group, multiplied by universal scaling factors that account for

DOI: 10.1021/jacs.6b12210
J. Am. Chem. Soc. 2017, 139, 3052−3064

the departure of the order of the hydroxyl groups from perfectly hexagonal and the fluctuations of the hydroxyl groups in and out of the plane of the surface. We find that both structural mismatch and fluctuations decrease the freezing efficiency of ice-nucleating surfaces.

In agreement with previous interpretation of experimental data,[33] we conclude that monolayers of *n*-alkyl alcohols are more efficient ice nucleants than are monolayers of fatty acids because for a given chain length they produce more compact monolayers that have better structural matching to the basal plane of ice. The simulations indicate that fluctuations decrease by half the freezing efficiency of alcohol monolayers with respect to that predicted from lattice matching alone. We interpret that fluctuations decrease the freezing efficiency because they increase the curvature or roughness of the surface, which have deleterious effects on ice nucleation.[42,43]

From the simulations of freezing by alcohol monolayers, we build a master curve to predict the freezing efficiency of hydroxylated organic surfaces as a function of their fluctuations and structural mismatch to ice. The master curve faithfully reproduces the freezing efficiencies measured in the simulations and correctly predicts the evolution of the experimental freezing efficiencies of alcohols and acids with chain length. The master curve, however, underestimates the freezing efficiencies of these surfaces. We demonstrate that this is due to a systematic underestimation of the binding free energies of ice to the alcohol and acid monolayers by the simulation model, which could arise from invalidity of some approximations of CNT, a larger effective curvature of the finite surface in simulations than in experiments, or the water−alcohol force field in the simulations. An assessment of the effect of the force field indicates that the freezing efficiency of the surface increases with the strength of the water−hydroxyl interaction and decreases with increasing attraction of water to the hydrocarbon moieties. The theoretical framework we provide to relate the freezing efficiency of a surface to its binding free energy is a powerful tool that can be extended to the analysis and prediction of the nonequilibrium ice-freezing efficiency of any surface from an equilibrium property that can be measured in simulations or experiments.

This work provides a relationship between the order and fluctuations of ice-nucleating surfaces, the structure of water intercalated with the monolayer, the thermodynamics of binding of ice to the surface, and the heterogeneous crystallization temperature of ice. Preordered domains of interfacial water with ice-like order have been identified in simulations[41−43,45,46,51,55,59] and experiments[48] of ice-nucleating surfaces. These preordered domains are the birthplace of ice on carbon surfaces and decrease the nucleation barrier through stabilization of the ice crystallites.[42,43,46] Likewise, we find that regularly hydroxylated organic surfaces can order interfacial water to produce domains of ice-like hexagons, and that these preordered domains are the birthplace of ice. The ice-like domains on alcohol monolayers are formed by the hydroxyl groups from the alcohols intercalated with interfacial waters from the liquid. The ice nuclei hydrogen bond directly to the intercalated water molecules. Importantly, the topography of the intercalated water layer in the ice-like domains is smoother than nonordered regions of the surface, which facilitates the nucleation of the ice crystals. Increasing the flexibility of the surface or structural mismatch to ice results in smaller ice-like domains, rougher water interface, weaker binding to ice, and poorer ice nucleation ability of the surface. The identification of spectroscopic signatures associated with the ice-like ordering of interfacial water[25,32,48,149] suggests that it may be possible to predict ice-freezing efficiency of ice-nucleating surfaces quantitatively from the spectra of interfacial water.

AUTHOR INFORMATION

Corresponding Author

*E-mail: Valeria.Molinero@utah.edu.

ORCID

Valeria Molinero: 0000-0002-8577-4675

Notes

The authors declare no competing financial interest.

ACKNOWLEDGMENTS

We acknowledge valuable discussions with Dr. Tom Hill from Colorado State University and Prof. Ryan Steele from The University of Utah. This work was supported by the National Science Foundation through award CHE-1305427 "Center for Aerosol Impacts on Climate and the Environment" and by the Natural Sciences and Engineering Research Council of Canada through award 249934-2012. We thank the Center for High Performance Computing at The University of Utah for technical support and a grant of computer time.

REFERENCES

(1) Meyers, M. P.; DeMott, P. J.; Cotton, W. R. *J. Appl. Meteorol.* **1992**, *31*, 708−721.

(2) Koop, T.; Luo, B.; Tsias, A.; Peter, T. *Nature* **2000**, *406*, 611−614.

(3) DeMott, P. J. *J. Appl. Meteorol.* **1990**, *29*, 1072−1079.

(4) Pruppacher, H. R.; Klett, J. D.; Wang, P. K. *Aerosol Sci. Technol.* **1998**, *28*, 381−382.

(5) Kumaki, Y.; Kawano, K.; Hikichi, K.; Matsumoto, T.; Matsushima, N. *Biochem. Biophys. Res. Commun.* **2008**, *371*, 5−9.

(6) Tinsley, B. A.; Rohrbaugh, R. P.; Hei, M.; Beard, K. V. *J. Atmos. Sci.* **2000**, *57*, 2118−2134.

(7) Tinsley, B. A.; Rohrbaugh, R. P.; Hei, M. *Atmos. Res.* **2001**, *59−60*, 115−135.

(8) Christner, B. C.; Morris, C. E.; Foreman, C. M.; Cai, R.; Sands, D. C. *Science* **2008**, *319*, 1214−1214.

(9) Heymsfield, A. J. *J. Atmos. Sci.* **1977**, *34*, 367−381.

(10) Hiron, T.; Flossmann, A. I. *J. Atmos. Sci.* **2015**, *72*, 3322−3339.

(11) Hill, T. C. J.; Moffett, B. F.; DeMott, P. J.; Georgakopoulos, D. G.; Stump, W. L.; Franc, G. D. *Appl. Microbiol.* **2014**, *80*, 1256−1267.

(12) Murray, B. J.; Broadley, S. L.; Wilson, T. W.; Bull, S. J.; Wills, R. H.; Christenson, H. K.; Murray, E. J. *Phys. Chem. Chem. Phys.* **2010**, *12*, 10380−10387.

(13) Murray, B. J.; O'Sullivan, D.; Atkinson, J. D.; Webb, M. E. *Chem. Soc. Rev.* **2012**, *41*, 6519−6554.

(14) Hoose, C.; Kristjánsson, J. E.; Chen, J.-P.; Hazra, A. *J. Atmos. Sci.* **2010**, *67*, 2483−2503.

(15) DeMott, P. J.; Hill, T. C. J.; McCluskey, C. S.; Prather, K. A.; Collins, D. B.; Sullivan, R. C.; Ruppel, M. J.; Mason, R. H.; Irish, V. E.; Lee, T.; Hwang, C. Y.; Rhee, T. S.; Snider, J. R.; McMeeking, G. R.; Dhaniyala, S.; Lewis, E. R.; Wentzell, J. J. B.; Abbatt, J.; Lee, C.; Sultana, C. M.; Ault, A. P.; Axson, J. L.; Diaz Martinez, M.; Venero, I.; Santos-Figueroa, G.; Stokes, M. D.; Deane, G. B.; Mayol-Bracero, O. L.; Grassian, V. H.; Bertram, T. H.; Bertram, A. K.; Moffett, B. F.; Franc, G. D. *Proc. Natl. Acad. Sci. U. S. A.* **2016**, *113*, 5797−5803.

(16) DeMott, P. J.; Prenni, A. J.; Liu, X.; Kreidenweis, S. M.; Petters, M. D.; Twohy, C. H.; Richardson, M. S.; Eidhammer, T.; Rogers, D. C. *Proc. Natl. Acad. Sci. U. S. A.* **2010**, *107*, 11217−11222.

(17) DeMott, P. J.; Cziczo, D. J.; Prenni, A. J.; Murphy, D. M.; Kreidenweis, S. M.; Thomson, D. S.; Borys, R.; Rogers, D. C. *Proc. Natl. Acad. Sci. U. S. A.* **2003**, *100*, 14655−14660.

(18) Fukuta, N. *J. Atmos. Sci.* **1966**, *23*, 191−196.

DOI: 10.1021/jacs.6b12210
J. Am. Chem. Soc. 2017, 139, 3052−3064

(19) Wang, B.; Lambe, A. T.; Massoli, P.; Onasch, T. B.; Davidovits, P.; Worsnop, D. R.; Knopf, D. A. *J. Geophys. Res.* **2012**, *117*, 2156−2202.
(20) Edwards, G. R.; Evans, L. F. *J. Atmos. Sci.* **1971**, *28*, 1443−1447.
(21) Hoose, C.; Kristjánsson, J. E.; Burrows, S. M. *Environ. Res. Lett.* **2010**, *5*, 024009.
(22) Pratt, K. A.; DeMott, P. J.; French, J. R.; Wang, Z.; Westphal, D. L.; Heymsfield, A. J.; Twohy, C. H.; Prenni, A. J.; Prather, K. A. *Nat. Geosci.* **2009**, *2*, 398−401.
(23) Davies, P. L. *Trends Biochem. Sci.* **2014**, *39*, 548−555.
(24) Gavish, M.; Popovitz-Biro, R.; Lahav, M.; Leiserowitz, L. *Science* **1990**, *250*, 973−975.
(25) Ochshorn, E.; Cantrell, W. *J. Chem. Phys.* **2006**, *124*, 054714.
(26) Jacquemain, D.; Leveiller, F.; Weinbach, S. P.; Lahav, M.; Leiserowitz, L.; Kjaer, K.; Als-Nielsen, J. *J. Am. Chem. Soc.* **1991**, *113*, 7684−7691.
(27) Majewski, J.; Popovitz-Biro, R.; Bouwman, W. G.; Kjaer, K.; Als-Nielsen, J.; Lahav, M.; Leiserowitz, L. *Chem. - Eur. J.* **1995**, *1*, 304−311.
(28) Majewski, J.; Popovitz-Biro, R.; Kjaer, K.; Als-Nielsen, J.; Lahav, M.; Leiserowitz, L. *J. Phys. Chem.* **1994**, *98*, 4087−4093.
(29) Seeley, L. H.; Seidler, G. T. *J. Chem. Phys.* **2001**, *114*, 10464−10470.
(30) Seeley, L. H.; Seidler, G. T. *Phys. Rev. Lett.* **2001**, *87*, 055702.
(31) Davey, R. J.; Maginn, S. J.; Steventon, R. B.; Ellery, J. M.; Murrell, A. V.; Booth, J.; Godwin, A. D.; Rout, J. E. *Langmuir* **1994**, *10*, 1673−1675.
(32) Du, Q.; Superfine, R.; Freysz, E.; Shen, Y. *Phys. Rev. Lett.* **1993**, *70*, 2313−2316.
(33) Popovitz-Biro, R.; Wang, J. L.; Majewski, J.; Shavit, E.; Leiserowitz, L.; Lahav, M. *J. Am. Chem. Soc.* **1994**, *116*, 1179−1191.
(34) Knopf, D. A.; Forrester, S. M. *J. Phys. Chem. A* **2011**, *115*, 5579−5591.
(35) Liou, Y. C.; Tocilj, A.; Davies, P. L.; Jia, Z. *Nature* **2000**, *406*, 322−324.
(36) Garnham, C. P.; Campbell, R. L.; Davies, P. L. *Proc. Natl. Acad. Sci. U. S. A.* **2011**, *108*, 7363−7367.
(37) Garnham, C. P.; Campbell, R. L.; Walker, V. K.; Davies, P. L. *BMC Struct. Biol.* **2011**, *11*, 36.
(38) Schmid, D.; Pridmore, D.; Capitani, G.; Battistutta, R.; Neeser, J.-R.; Jann, A. *FEBS Lett.* **1997**, *414*, 590−594.
(39) Liu, K.; Wang, C.; Ma, J.; Shi, G.; Yao, X.; Fang, H.; Song, Y.; Wang, J. *Proc. Natl. Acad. Sci. U. S. A.* **2016**, *113*, 14739−14744.
(40) Zobrist, B.; Koop, T.; Luo, B. P.; Marcolli, C.; Peter, T. *J. Phys. Chem. C* **2007**, *111*, 2149−2155.
(41) Zielke, S. A.; Bertram, A. K.; Patey, G. N. *J. Phys. Chem. B* **2016**, *120*, 1726−1734.
(42) Lupi, L.; Hudait, A.; Molinero, V. *J. Am. Chem. Soc.* **2014**, *136*, 3156−3164.
(43) Lupi, L.; Molinero, V. *J. Phys. Chem. A* **2014**, *118*, 7330−7337.
(44) Evans, L. F. *Nature* **1967**, *213*, 384−385.
(45) Zielke, S. A.; Bertram, A. K.; Patey, G. N. *J. Phys. Chem. B* **2015**, *119*, 9049−9055.
(46) Lupi, L.; Peters, B.; Molinero, V. *J. Chem. Phys.* **2016**, *145*, 211910.
(47) Cox, S. J.; Kathmann, S. M.; Slater, B.; Michaelides, A. *J. Chem. Phys.* **2015**, *142*, 184705.
(48) Abdelmonem, A.; Lützenkirchen, J.; Leisner, T. *Atmos. Meas. Tech.* **2015**, *8*, 3519−3526.
(49) Moore, E. B.; Molinero, V. *Nature* **2011**, *479*, 506−508.
(50) Moore, E. B.; Molinero, V. *J. Chem. Phys.* **2010**, *132*, 244504.
(51) Reinhardt, A.; Doye, J. P. K. *J. Chem. Phys.* **2014**, *141*, 084501.
(52) Espinosa, J. R.; Vega, C.; Valeriani, C.; Sanz, E. *J. Chem. Phys.* **2016**, *144*, 034501.
(53) Zaragoza, A.; Conde, M. M.; Espinosa, J. R.; Valeriani, C.; Vega, C.; Sanz, E. *J. Chem. Phys.* **2015**, *143*, 134504.
(54) Espinosa, J. R.; Sanz, E.; Valeriani, C.; Vega, C. *J. Chem. Phys.* **2014**, *141*, 18C529.
(55) Bi, Y.; Cabriolu, R.; Li, T. *J. Phys. Chem. C* **2016**, *120*, 1507−1514.
(56) Cabriolu, R.; Li, T. *Phys. Rev. E* **2015**, *91*, 052402.
(57) Cox, S. J.; Raza, Z.; Kathmann, S. M.; Slater, B.; Michaelides, A. *Faraday Discuss.* **2014**, *167*, 389−403.
(58) Cox, S. J.; Kathmann, S. M.; Slater, B.; Michaelides, A. *J. Chem. Phys.* **2015**, *142*, 184704.
(59) Fitzner, M.; Sosso, G. C.; Cox, S. J.; Michaelides, A. *J. Am. Chem. Soc.* **2015**, *137*, 13658−13669.
(60) Sanz, E.; Vega, C.; Espinosa, J. R.; Caballero-Bernal, R.; Abascal, J. L. F.; Valeriani, C. *J. Am. Chem. Soc.* **2013**, *135*, 15008−15017.
(61) Fraux, G.; Doye, J. P. K. *J. Chem. Phys.* **2014**, *141*, 216101.
(62) Reinhardt, A.; Doye, J. P. K. *J. Chem. Phys.* **2012**, *136*, 054501.
(63) Haji-Akbari, A.; Debenedetti, P. G. *Proc. Natl. Acad. Sci. U. S. A.* **2015**, *112*, 10582−10588.
(64) Matsumoto, M.; Saito, S.; Ohmine, I. *Nature* **2002**, *416*, 409−413.
(65) Quigley, D.; Rodger, P. M. *J. Chem. Phys.* **2008**, *128*, 154518.
(66) Sosso, G. C.; Li, T.; Donadio, D.; Tribello, G. A.; Michaelides, A. *J. Phys. Chem. Lett.* **2016**, *7*, 2350−2355.
(67) Zhang, X.-X.; Chen, M.; Fu, M. *J. Chem. Phys.* **2014**, *141*, 124709.
(68) Yan, J. Y.; Patey, G. N. *J. Phys. Chem. Lett.* **2011**, *2*, 2555−2559.
(69) Yan, J. Y.; Patey, G. N. *J. Chem. Phys.* **2013**, *139*, 144501.
(70) Yan, J. Y.; Patey, G. N. *J. Phys. Chem. A* **2012**, *116*, 7057−7064.
(71) Małolepsza, E.; Keyes, T. *J. Chem. Theory Comput.* **2015**, *11*, 5613−5623.
(72) Sosso, G. C.; Chen, J.; Cox, S. J.; Fitzner, M.; Pedevilla, P.; Zen, A.; Michaelides, A. *Chem. Rev.* **2016**, *116*, 7078−7116.
(73) Pluhařová, E.; Vrbka, L.; Jungwirth, P. *J. Phys. Chem. C* **2010**, *114*, 7831−7838.
(74) Zielke, S. A.; Bertram, A. K.; Patey, G. N. *J. Phys. Chem. B* **2016**, *120*, 2291−2299.
(75) Haji-Akbari, A.; DeFever, R. S.; Sarupria, S.; Debenedetti, P. G. *Phys. Chem. Chem. Phys.* **2014**, *16*, 25916−25927.
(76) Glatz, B.; Sarupria, S. *J. Chem. Phys.* **2016**, *145*, 211924.
(77) Sosso, G. C.; Colombo, J.; Behler, J. r.; Del Gado, E.; Bernasconi, M. *J. Phys. Chem. B* **2014**, *118*, 13621−13628.
(78) Plimpton, S. *J. Comput. Phys.* **1995**, *117*, 1−19.
(79) Nosé, S. *J. Chem. Phys.* **1984**, *81*, 511−519.
(80) Hoover, W. G. *Phys. Rev. A: At., Mol., Opt. Phys.* **1985**, *31*, 1695−1697.
(81) Molinero, V.; Moore, E. B. *J. Phys. Chem. B* **2009**, *113*, 4008−4016.
(82) Malkin, T. L.; Murray, B. J.; Salzmann, C. G.; Molinero, V.; Pickering, S. J.; Whale, T. F. *Phys. Chem. Chem. Phys.* **2015**, *17*, 60−76.
(83) Moore, E. B.; Molinero, V. *Phys. Chem. Chem. Phys.* **2011**, *13*, 20008−20016.
(84) Moore, E. B.; de la Llave, E.; Welke, K.; Scherlis, D. A.; Molinero, V. *Phys. Chem. Chem. Phys.* **2010**, *12*, 4124−4134.
(85) Solveyra, E. G.; Llave, E. d. l.; Molinero, V.; Soler-Illia, G. J. A. A.; Scherlis, D. A. *J. Phys. Chem. C* **2013**, *117*, 3330−3342.
(86) Hudait, A.; Molinero, V. *J. Am. Chem. Soc.* **2014**, *136*, 8081−8093.
(87) Johnston, J. C.; Molinero, V. *J. Am. Chem. Soc.* **2012**, *134*, 6650−6659.
(88) Lu, J.; Qiu, Y.; Baron, R.; Molinero, V. *J. Chem. Theory Comput.* **2014**, *10*, 4104−4120.
(89) Moore, E. B.; Allen, J. T.; Molinero, V. *J. Phys. Chem. C* **2012**, *116*, 7507−7514.
(90) Moore, E. B.; Molinero, V. *J. Chem. Phys.* **2009**, *130*, 244505.
(91) Hujo, W.; Shadrack Jabes, B.; Rana, V. K.; Chakravarty, C.; Molinero, V. *J. Stat. Phys.* **2011**, *145*, 293−312.
(92) Kastelowitz, N.; Johnston, J. C.; Molinero, V. *J. Chem. Phys.* **2010**, *132*, 124511.
(93) Xu, L.; Molinero, V. *J. Phys. Chem. B* **2011**, *115*, 14210−14216.
(94) Nguyen, A. H.; Molinero, V. *J. Phys. Chem. B* **2015**, *119*, 9369−9376.
(95) Nguyen, A. H.; Koc, M. A.; Shepherd, T. D.; Molinero, V. *J. Phys. Chem. C* **2015**, *119*, 4104−4117.

DOI: 10.1021/jacs.6b12210
J. Am. Chem. Soc. 2017, 139, 3052−3064

(96) Holten, V.; Limmer, D. T.; Molinero, V.; Anisimov, M. A. *J. Chem. Phys.* **2013**, *138*, 174501.
(97) Bullock, G.; Molinero, V. *Faraday Discuss.* **2014**, *167*, 371−388.
(98) González Solveyra, E. a.; de la Llave, E.; Scherlis, D. A.; Molinero, V. *J. Phys. Chem. B* **2011**, *115*, 14196−14204.
(99) Lupi, L.; Kastelowitz, N.; Molinero, V. *J. Chem. Phys.* **2014**, *141*, 18C508.
(100) Jacobson, L. C.; Molinero, V. *J. Phys. Chem. B* **2010**, *114*, 7302−7311.
(101) Factorovich, M. H.; Molinero, V.; Scherlis, D. A. *J. Chem. Phys.* **2014**, *140*, 064111.
(102) Factorovich, M. H.; Molinero, V.; Scherlis, D. A. *J. Am. Chem. Soc.* **2014**, *136*, 4508−4514.
(103) Limmer, D. T.; Chandler, D. *J. Chem. Phys.* **2011**, *135*, 134503.
(104) Limmer, D. T.; Chandler, D. *J. Chem. Phys.* **2013**, *138*, 214504.
(105) Li, T.; Donadio, D.; Russo, G.; Galli, G. *Phys. Chem. Chem. Phys.* **2011**, *13*, 19807−19813.
(106) Jacobson, L. C.; Molinero, V. *J. Phys. Chem. B* **2010**, *114*, 7302−7311.
(107) Dhabal, D.; Nguyen, A. H.; Singh, M.; Khatua, P.; Molinero, V.; Bandyopadhyay, S.; Chakravarty, C. *J. Chem. Phys.* **2015**, *143*, 164512.
(108) Singh, M.; Dhabal, D.; Nguyen, A. H.; Molinero, V.; Chakravarty, C. *Phys. Rev. Lett.* **2014**, *112*, 147801.
(109) Hudait, A.; Qiu, S.; Lupi, L.; Molinero, V. *Phys. Chem. Chem. Phys.* **2016**, *18*, 9544−9553.
(110) Lupi, L.; Kastelowitz, N.; Molinero, V. *J. Chem. Phys.* **2014**, *141*, 18C508.
(111) Li, T.; Donadio, D.; Galli, G. *Nat. Commun.* **2013**, *4*, 1887.
(112) Lu, J.; Chakravarty, C.; Molinero, V. *J. Chem. Phys.* **2016**, *144*, 234507.
(113) Shadrack Jabes, B.; Nayar, D.; Dhabal, D.; Molinero, V.; Chakravarty, C. *J. Phys.: Condens. Matter* **2012**, *24*, 284116.
(114) Factorovich, M. H.; Gonzalez Solveyra, E.; Molinero, V.; Scherlis, D. A. *J. Phys. Chem. C* **2014**, *118*, 16290−16300.
(115) Limmer, D. T.; Chandler, D. *J. Chem. Phys.* **2012**, *137*, 044509.
(116) Jorgensen, W. L.; Madura, J. D.; Swenson, C. J. *J. Am. Chem. Soc.* **1984**, *106*, 6638−6646.
(117) Qiu, Y.; Molinero, V. *J. Am. Chem. Soc.* **2015**, *137*, 10642−10651.
(118) Krone, M.; Stone, J. E.; Ertl, T.; Schulten, K. *EuroVis-Short Papers* **2012**, *1*, 67−71.
(119) Humphrey, W.; Dalke, A.; Schulten, K. *J. Mol. Graphics* **1996**, *14*, 33−38.
(120) QuickSurf. In *VMD User's Guide*, version 1.9.3; NIH Biomedical Research Center for Macromolecular Modeling and Bioinformatics: Urbana, IL, 2016. http://www.ks.uiuc.edu/Research/vmd/ (accessed on December 30, 2016).
(121) Iannone, R.; Chernoff, D. I.; Pringle, A.; Martin, S. T.; Bertram, A. K. *Atmos. Chem. Phys.* **2011**, *11*, 1191−1201.
(122) Wheeler, M. J.; Mason, R. H.; Steunenberg, K.; Wagstaff, M.; Chou, C.; Bertram, A. K. *J. Phys. Chem. A* **2015**, *119*, 4358−4372.
(123) Turnbull, D.; Fisher, J. C. *J. Chem. Phys.* **1949**, *17*, 71−73.
(124) Koop, T.; Murray, B. J. *J. Chem. Phys.* **2016**, *145*, 211915.
(125) Jacobson, L. C.; Hujo, W.; Molinero, V. *J. Phys. Chem. B* **2009**, *113*, 10298−10307.
(126) Turnbull, D. *J. Appl. Phys.* **1950**, *21*, 1022−1028.
(127) Jahnert, S.; Vaca Chavez, F.; Schaumann, G. E.; Schreiber, A.; Schonhoff, M.; Findenegg, G. H. *Phys. Chem. Chem. Phys.* **2008**, *10*, 6039−51.
(128) Ketcham, W. M.; Hobbs, P. V. *Philos. Mag.* **1969**, *19*, 1161−1173.
(129) Hardy, S. C. *Philos. Mag.* **1977**, *35*, 471−484.
(130) Limmer, D. T.; Chandler, D. *J. Chem. Phys.* **2012**, *137*, 044509.
(131) Limmer, D. T.; Chandler, D. *J. Chem. Phys.* **2014**, *141*, 18C505.
(132) Espinosa, J. R.; Vega, C.; Sanz, E. *J. Phys. Chem. C* **2016**, *120*, 8068−8075.
(133) Espinosa, J. R.; Vega, C.; Valeriani, C.; Sanz, E. *J. Chem. Phys.* **2016**, *144*, 034501.
(134) Lupi, L.; Hudait, A.; Peters, B.; Grünwald, M.; Gotchy Mullen, R.; Nguyen, A. H.; Molinero, V. *Nature* **2017**, submitted for publication.
(135) Young, T. *Philos. Trans. R. Soc. London* **1805**, *95*, 65−87.
(136) Berge, B.; Renault, A. *EPL* **1993**, *21*, 773.
(137) Auer, S.; Frenkel, D. *Phys. Rev. Lett.* **2003**, *91*, 015703.
(138) Iwamatsu, M. *Langmuir* **2015**, *31*, 3861−3868.
(139) Iwamatsu, M. Heterogeneous Nucleation on a Completely Wettable Substrate. In *Advances in Contact Angle, Wettability and Adhesion*; John Wiley & Sons, Inc.: Salem, MA, 2013; pp 49−72.
(140) Yue, X.; Dobner, B.; Iimura, K.-i.; Kato, T.; Möhwald, H.; Brezesinski, G. *J. Phys. Chem. B* **2006**, *110*, 22237−22244.
(141) Pruppacher, H. R.; Klett, J. D. *Microphysics of Clouds and Precipitation*; Springer Science & Business Media: Dordrecht, 2010.
(142) Malkin, T. L.; Murray, B. J.; Brukhno, A. V.; Anwar, J.; Salzmann, C. G. *Proc. Natl. Acad. Sci. U. S. A.* **2012**, *109*, 1041−1045.
(143) Fileti, E. E.; Chaudhuri, P.; Canuto, S. *Chem. Phys. Lett.* **2004**, *400*, 494−499.
(144) Moreno-Calvo, E.; Gbabode, G.; Cordobilla, R.; Calvet, T.; Cuevas-Diarte, M. A.; Negrier, P.; Mondieig, D. *Chem. - Eur. J.* **2009**, *15*, 13141−13149.
(145) Lin, W.; Clark, A. J.; Paesani, F. *Langmuir* **2015**, *31*, 2147−2156.
(146) Tang, C. Y.; Allen, H. C. *J. Phys. Chem. A* **2009**, *113*, 7383−7393.
(147) Adams, E. M.; Allen, H. C. *Atmosphere* **2013**, *4*, 315−336.
(148) Lee, K. Y. C.; Majewski, J.; Kuhl, T. L.; Howes, P. B.; Kjaer, K.; Lipp, M. M.; Waring, A. J.; Zasadzinski, J. A.; Smith, G. S. *Biophys. J.* **2001**, *81*, 572−585.
(149) Weissbuch, I.; Leiserowitz, L.; Lahav, M. *Curr. Opin. Colloid Interface Sci.* **2008**, *13*, 12−22.

DOI: 10.1021/jacs.6b12210
J. Am. Chem. Soc. 2017, 139, 3052−3064